

Rethinking Few-Shot Image Fusion: Granular Ball Priors Enable General-Purpose Deep Fusion

Minjie Deng, Yan Wei*, An Wu, Yuncan Ouyang, Hao Zhai, Qian Yao Peng

Abstract—In image fusion tasks, due to the absence of real fused images as priors, most deep learning approaches rely on large-scale paired datasets to extract global weighting features or generate pseudo-supervised images through algorithmic constructions. Unlike previous methods, this paper re-examines the training paradigm of prior-guided networks under few-shot conditions and introduces rough set theory, where the algorithm is regarded as a prior generator while the network re-infers and adaptively optimizes the prior through the loss function. As a result, the inference burden of the neural network is reduced, enabling effective few-shot learning. To provide the prior, we propose the Granular Ball Pixel Computation (GBPC) algorithm. This algorithm first models pixel pairs of the fused image in the luminance subspace using meta-granular balls, and mines intra-ball information across multiple granular levels. At the fine-grained level, sliding granular balls assign adaptive weights to pixels within each meta-granular ball, achieving pixel-level fusion as a prior. At the coarse-grained level, the algorithm performs split computation within a single image to estimate the distributions of positive and boundary domains of meta-granular balls, thereby enabling modality awareness and computing prior confidence, which dynamically guides the weighting of the loss function. The network structure and the algorithmic prior are coupled through the loss function to form an integrated framework. Thanks to the dynamic weighting mechanism, the network can adaptively adjust to different priors during training, enhancing its perception and fusion capability across modalities. Based on this design, we name the proposed framework GBFF (Granular Ball Fusion Framework). Experiments on four fusion tasks demonstrate that even with only ten training image pairs per task, GBFF achieves superior performance in both visual quality and model compactness. Our code is publicly available at: <https://github.com/DMinjie/GBFF>

Index Terms—Image fusion, Granular Ball, Few-shot, Deep learning, Rough set

I. INTRODUCTION

DUE to the inherent limitations of sensors, images captured by a single sensor often have restricted representational capacity and cannot effectively capture all the information within the scene. The goal of image fusion is to combine the information from images acquired by different sensors, integrating multiple modalities into a single image that contains richer and more comprehensive information. For example, visible-light images captured at night cannot record thermal sources in dark regions, whereas their fusion with infrared images can effectively enhance the representation of thermal information. Because the fused image integrates the advantages of multiple sensing devices, it has found broad applications in fields such as medical imaging, security surveillance, target recognition, and image segmentation.

In previous research, significant progress has been made in areas such as multi-focus image fusion, multi-exposure image

fusion, infrared and visible image fusion, and medical image fusion. These methods can generally be divided into traditional approaches and deep learning-based approaches. Traditional methods typically decompose images using algorithmic operations at different scales or spatial domains to extract features for fusion[1]. However, as practical requirements in real-world scenarios have grown, the design of these algorithms has become increasingly complex. Consequently, deep learning methods have gradually become dominant. Among them, deep learning-based approaches can be categorized into convolutional neural network (CNN)-based methods, generative adversarial network (GAN)-based methods, Transformer-based methods, diffusion model-based methods, and hybrid approaches that integrate traditional algorithms with deep learning. These approaches have achieved remarkable results in the field[2]. Traditional methods provide priors that guide neural networks to form semi-manual fusion rules, which has been proven effective in enhancing the expressive power of fused images—for example, through wavelet transforms, multi-scale decompositions, and saliency-based techniques. However, previous hybrid methods that combine traditional algorithms with deep learning often relied on fixed loss functions to learn supervised images derived from traditional methods as complete priors, lacking the coupling and adaptability between algorithms and networks. As a result, a large number of training samples are still required for convergence, making few-shot training difficult to achieve.

To address the aforementioned challenges, we introduce the concept of granular balls from rough set theory into the field of image fusion, and design a fusion framework capable of adaptively adjusting both priors and loss functions based on the training samples. Specifically, we first perform granular modeling on the training images and propose the Granular Ball Pixel Computation (GBPC) algorithm as a prior generator. At the fine-grained level, GBPC computes pixel weights within each meta-granular ball through sliding operations, thereby achieving pixel-level fusion and generating an initial supervised image as the prior. At the coarse-grained level, GBPC calculates the distributions of meta-granular balls in the positive and boundary domains of the current image through a splitting process. After modality perception, these distributions determine the final weighting of the loss function. The ratio of the positive domain indicates the proportion of high-confidence meta-granular balls contained in the current prior image, thereby defining the confidence level of the prior. Together with the boundary domain ratio, it dynamically adjusts the loss weighting for each training sample. Within this framework, the neural network re-infers and adaptively

optimizes the prior through the loss function. Consequently, the prior image can be regarded as a degraded image carrying partially correct fusion information, while the neural network performs the inference process from the original paired inputs to the true fused image based on the known prior. In summary, for each pair of input images, the Granular Ball Pixel Computation algorithm provides an incomplete prior, and the neural network performs re-inference based on this incomplete prior to establish the mapping capability from raw inputs to the fused image. Under this design, the network effectively avoids the overfitting problem caused by complete priors and can be efficiently trained even with few samples. Our main contributions can be summarized as follows:

- For multi-source image fusion, we propose an adaptive few-shot fusion framework that integrates algorithmic priors with neural networks. The algorithm provides an incomplete prior, while the neural network performs re-inference based on this known prior through an adaptive loss function, thereby achieving few-shot learning.
- For the first time, rough set theory is employed to model the image fusion task, and the Granular Ball Pixel Computation (GBPC) algorithm is proposed. This algorithm mines the internal information of meta-granular balls through granular ball operations — at the fine-grained level, it provides priors for pixel-level fusion, while at the coarse-grained level, it computes the determinacy and indeterminacy of the prior, thereby achieving modality perception and adaptive loss function adjustment.
- The effectiveness of incomplete priors in image fusion is revealed, and the differences between complete and incomplete priors are analyzed, providing a new perspective for the design of priors in fusion algorithms.
- Comprehensive qualitative and quantitative comparisons with state-of-the-art (SOTA) methods are conducted across multiple fusion tasks. Despite using only ten images for training, the proposed method achieves clear advantages in both fusion image quality and deployment cost, demonstrating strong generalization ability and ease of deployment.

The structure of the remaining sections is organized as follows. In Section 2, we introduce existing image fusion methods and the fundamentals of granular computing. Section 3 provides a detailed description of the proposed fusion framework and algorithmic implementation. In Section 4, we present comparative analyses between our method and existing approaches. Finally, Section 5 offers further theoretical discussions and extensive experimental validations.

II. RELATED WORK

In this section, we will introduce the methods and developments of image fusion, as well as the theory and applications of granular computing.

A. Image Fusion

Image fusion requires methods capable of extracting features from different modalities and highlighting the effective information contributed by each modality after fusion, thereby

fully representing the real scene [3]. In previous studies, researchers mainly adopted approaches such as multi-scale transformations, subspace analysis, and sparse representation. As application scenarios became increasingly complex, some researchers started combining multiple techniques to further enhance information extraction capability [4]. Early studies utilized the Laplacian Pyramid (LP) to decompose images into multiple frequency bands, followed by the introduction of the Dual-Tree Complex Wavelet Transform (DWCWT), which extracts effective information via different filtering operations. However, wavelet-based methods exhibit poor edge extraction performance, motivating the development of curvelet transform (Curvelet), which captures edge structures more effectively. To enhance the representation of structural information in fusion, Guided Filtering (GFF) was also incorporated into image fusion [5]. In addition, Liu et al. combined sparse matrix representation with traditional transform methods and achieved promising results in extracting effective fusion information [6].

However, in real-world applications, as the usage demands increase, image processing algorithms often suffer from limited generalization capability. This leads to increasingly complex algorithmic designs, posing significant challenges for practical deployment [4]. With the rise of deep learning, Li et al. introduced it into the field of image fusion for the first time [7], making it gradually become a mainstream research direction. Based on model architectures, the earliest encoder–decoder network, DeepFuse, demonstrated strong detail extraction capability for infrared and visible images [8]. Subsequently, IFCNN leveraged pre-trained networks to extract features and achieved general-purpose fusion within a CNN framework, while U2Fusion proposed a saliency-based loss function to implicitly guide cross-modality fusion. Unlike CNN-based methods, GAN-based architectures use a generator–discriminator mechanism to evaluate the fused outputs. FusionGAN [9] was the first to apply GANs to image fusion, and Ma et al. further proposed DDcGAN [10], where multiple discriminators were utilized to improve fusion accuracy. For Transformer-based architectures, long-range dependency modeling is exploited by decomposing images into tokens for processing [11]. On this basis, Ma et al. designed cross-domain attention using Swin Transformer to enhance fusion quality [12]. Furthermore, diffusion models have also been introduced into fusion tasks. Chen et al. developed a multi-exposure diffusion framework by designing flexible fusion strategies [13].

In addition to model-driven methods, approaches free from network constraints have also been proposed. By leveraging deep priors to perform sample-free fusion directly on images, ZMFF treats multi-focus masks as denoising priors to accomplish multi-focus fusion [14], while ZVIR directly utilizes the network structure to extract infrared and visible features, thus achieving image fusion without data dependence [15]. Bai et al. further proposed Refusion, which performs unsupervised fusion by meta-learning the loss function [16]. In addition, Wang et al. introduced a fusion method that combines vision–language models with image data [17]. With the development of deep learning, hybrid approaches that integrate traditional algorithms with neural networks have also emerged.

For example, MMIF-INET integrates wavelet decomposition with invertible networks for medical image fusion [18], while Wang et al. later proposed a semi-supervised fusion framework that combines Laplacian pyramid transformers with neural networks [19]. Moreover, Kang et al. extracted fusion features within Euclidean space and developed SMLNet based on this strategy [20].

Although these methods have achieved remarkable success, existing trainable fusion approaches inevitably rely on large-scale datasets to progressively update model parameters, while sample-free methods still suffer from high computational cost, making practical deployment challenging. Moreover, deep learning methods that depend on traditional priors often struggle to adaptively determine the fusion scale; even when prior information is incorporated, a substantial amount of external data is still required to constrain the learning of network parameters. These limitations collectively hinder the rapid deployment of image fusion techniques, especially in few-shot and real-world application scenarios.

B. Granular Ball Computing

Rough sets are widely used to model uncertainty in data, while ball granules offer a granulation-based approach to simplify fine-grained data, typically represented by a centroid and a radius within a spatial Granular Ball model [21], [22]. Building upon these foundations, researchers proposed the GBNRS method, which integrates granulation with approximation theory to handle continuous data more effectively [23]. Subsequently, Granular Ball clusters were introduced into clustering tasks to model instance relationships, leading to the Ball k-means algorithm, which significantly reduces spatial complexity during clustering [24]. Granular Ball computing has demonstrated strong potential in data analysis and uncertainty modeling[25]. However, in the field of image processing, due to the lack of a unified modeling framework, existing ball granule-based methods have struggled to effectively capture relationships between image regions or modalities.

III. PROPOSED METHODS

A. Framework

In our proposed framework, the training phase can be divided into two main parts: one involves generating incomplete priors using the Granular Ball Pixel Computation algorithm, and the other involves the neural network performing re-inference on the basis of these incomplete priors to obtain the final fused image. To verify the effectiveness of the proposed priors, we deliberately employ a simple CNN architecture without introducing any additional regularization modules such as attention mechanisms. This ensures that all information within the network is transmitted and regulated solely through the loss function. For each pair of training input images, the pixel pairs are first granulated to form meta-granular balls. The Granular Ball Pixel Computation algorithm then mines the internal information of each meta-granular ball and performs fusion to generate a pseudo-supervised image. Due to the algorithm's limited inference capacity, the resulting prior image contains incomplete information compared with the real

fused image. Therefore, we use rough set theory to describe the confidence of this prior, which allows us to regulate the loss function dynamically—achieving adaptive coupling between the algorithm and the network. In summary, each pair of input images possesses its own independent prior and loss function. After dividing the images into patches, a large number of independent and diverse samples can be generated, enabling the network to learn effectively even in a few-shot learning environment.

B. Definitions and Concepts

This algorithm operates in the luminance subspace. In previous image fusion studies, performing a series of processing steps and extracting feature information within the luminance subspace (YCBCR) has achieved numerous successful results[16], [26]. In fused images, the luminance of entities from different modalities exhibits continuity and similarity. Pixels with higher luminance generally contain greater information content, and such information is often relative. Based on this observation, we design the Granular Ball Pixel Algorithm, which uses the granular ball as a scale to explore the internal information of pixel pairs at both coarse and fine granularities, thereby evaluating the effectiveness of such information. Specifically, we granularize the pixel pairs from two input images to construct coordinate-based meta-granular Balls that describe the luminance of pixel pairs at corresponding positions. The definition of the meta-granular ball is given as Definition 1.

Definition 1. Meta-Granular Ball. A Meta-Granular Ball, denoted as $mG(x, y)$, represents the paired brightness values of two corresponding pixels at coordinate (x, y) from image A and image B . Formally, it can be expressed as:

$$mG(x, y) = \{L_A(x, y), L_B(x, y)\}, \quad (1)$$

where $L_A(x, y)$ and $L_B(x, y)$ denote the luminance intensities of images A and B at position (x, y) , respectively. This meta-granular ball serves as the *elementary unit* for subsequent granular-ball construction, providing the basis for local information interaction between the two modalities.

A granular ball serves as a spatial scale unit for evaluating the meta-granular ball. Its formal definition is given in Definition 2. Although, in the current brightness subspace, the granular ball behaves more like a hierarchical regional partition, its mathematical model in the spatial domain will gradually evolve into a true spherical structure once richer spatial information is introduced in the future.

Definition 2. Granular Ball We define a granular ball $\mathcal{G}(\mu, r)$ in the brightness space as:

$$\mathcal{G}(\mu, r) = \{x \in \mathbb{R} \mid |x - \mu| \leq r\}, \quad \mathcal{G}(\mu, r) \subseteq [0, 255] \quad (2)$$

where r denotes the radius of the granular ball, μ represents the center, \mathbb{R} is the real number domain, and x corresponds to any element within the meta-granular ball.

After the granular-ball processing, each meta-granular ball will eventually be categorized into the *positive domain* or the *boundary domain*, and the corresponding pixel masks

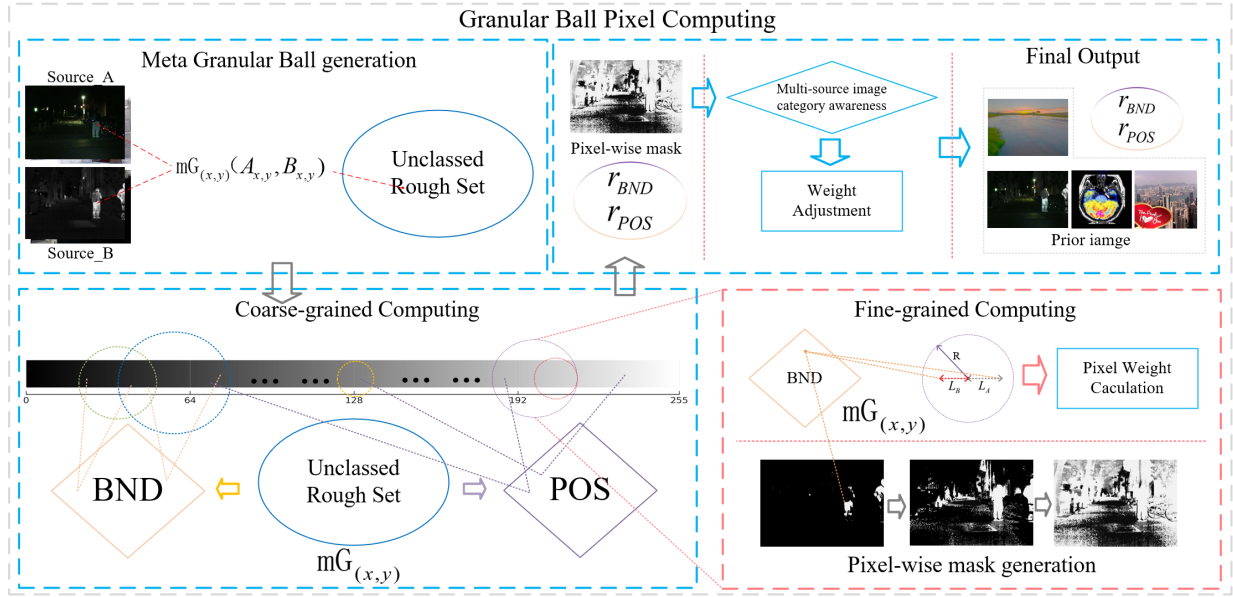


Fig. 1. Illustration of the Granular Ball Pixel Computing (GBPC) framework and visualization of the prior formation process.

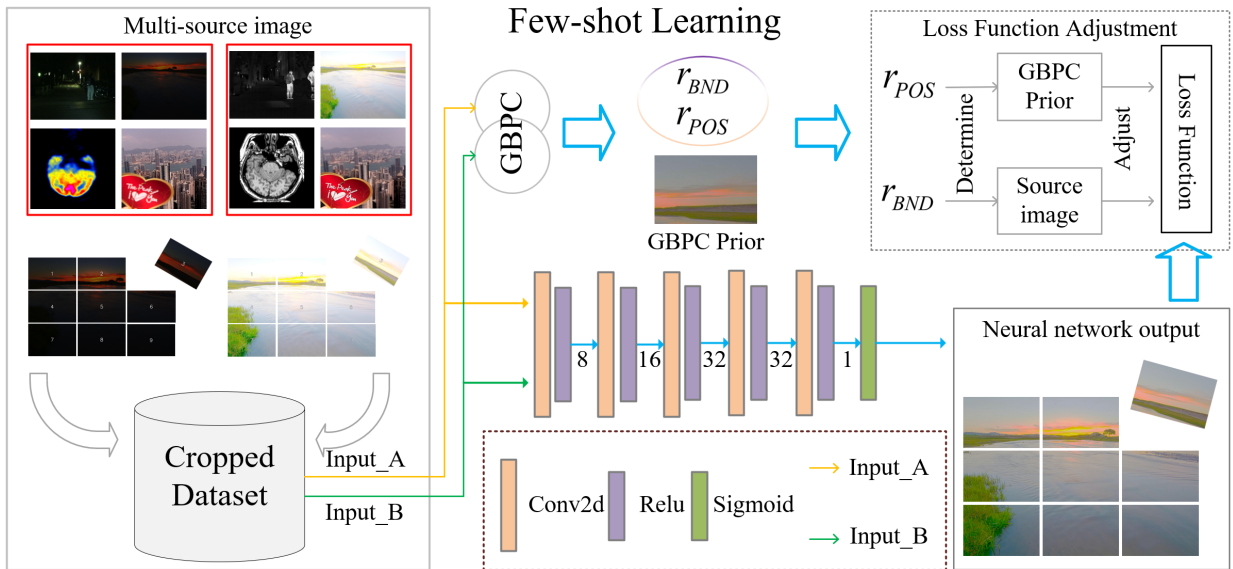


Fig. 2. Illustration of the network architecture and the processing steps involved during the learning procedure.

are computed during this process. The positive domain describes the meta-granular balls that are correctly evaluated, while the boundary domain corresponds to those undergoing uncertain evaluations. The formal definitions of the positive and boundary domains are given in Definition 3 and Definition 4, respectively.

Definition 3. Positive Domain(POS) During the process of granular-ball division, if there exists a meta-granular ball mG belonging to a granular ball $\mathcal{G}(\mu, r)$, and one of its elements lies within the splitting region while the other lies outside the granular ball, then mG is classified into the *positive domain*. Formally, the positive domain can be expressed as:

$$\text{POS} = \{mG \mid mG \in \mathcal{G}(\mu, r), x_1 \in \Omega_{\text{split}}, x_2 \notin \mathcal{G}(\mu, r)\}, \quad (3)$$

where Ω_{split} denotes the current splitting region, and (x_1, x_2) are the paired elements contained within mG .

Definition 4. Boundary Domain(BND) During the expansion process of the granular-ball radius, if there exists a meta-granular ball mG belonging to a granular ball $\mathcal{G}(\mu, r)$, and all elements of mG are located within the granular ball, then mG is classified into the *boundary domain*. Formally, the boundary domain can be expressed as:

$$\text{BND} = \{mG \mid mG \in \mathcal{G}(\mu, r), x_i \in \mathcal{G}(\mu, r), \forall x_i \in mG\}. \quad (4)$$

C. Granular Ball Pixel Computing

The granular ball is initialized at the boundary and begins executing the Granular Ball Pixel Computing algorithm, form-

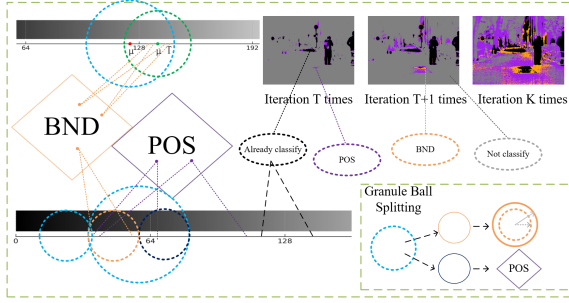


Fig. 3. Visualization of the meta-granular ball capturing process in Granular Ball Pixel Computing for clearer understanding.

ing both fine-grained and coarse-grained judgments. During its expansion and rolling process, the granular ball gradually captures meta-granular balls. The expansion of the granular ball increases its capture range by enlarging its radius, which can be described as follows:

$$\mathcal{G}_{t+1}(\mu, r) = \mathcal{G}_t(\mu, r + \Delta d) \quad (5)$$

where Δd denotes the incremental step length of radius expansion in each iteration.

The granular ball is encouraged to capture as many meta-granular balls as possible. Since it operates only in the luminance space, it slides along the boundary when vacancies appear at the boundary position, which can be mathematically described as follows:

$$\mathcal{G}_{t+1}(\mu, r) = \mathcal{G}_t(\mu + \Delta m, r + \Delta m/2) \quad (6)$$

where, Δm is determined by the elements of meta-granular balls that are closest to the boundary. The sliding process stops once an element of a meta-granular ball reaches the boundary of the granular ball.

When the granular ball expands to its maximum limit, a splitting process is triggered. Therefore, when $r \geq k\Delta d$, the granular ball undergoes division as follows:

$$\mathcal{G}_r(\mu, r) = \mathcal{G}_t(\mu - r/2, r/2) \in \Omega_{\text{split}}, \quad (7)$$

$$\mathcal{G}_{t+1}(\mu, r) = \mathcal{G}_t(\mu + r/2, r/2) \quad (8)$$

where, the split granular ball $\mathcal{G}_r(\mu, r)$ belongs to the splitting set Ω_{split} . According to the definition in Equation (3), the meta-granular balls contained within it are assigned to the positive domain (POS). The newly generated granular ball $\mathcal{G}(\mu, r)$ will continue to operate until all meta-granular balls are captured and classified.

During the process of capturing meta-granular balls, at the fine-grained level, the pixel pairs within the meta-granular balls located in the boundary domain are computed according to the following equation:

$$D = \max\{L_A(x, y), L_B(x, y)\}, \quad (9)$$

$$L = \max(|D - (\mu - r)|, |D - (\mu + r)|), \quad (10)$$

$$w(x, y) = \frac{L}{2r}, \quad (11)$$

$$X_A(x, y) = \begin{cases} w(x, y), & L_A(x, y) > L_B(x, y), \\ 1 - w(x, y), & L_A(x, y) \leq L_B(x, y), \end{cases} \quad (12)$$

$$X_B(x, y) = 1 - X_A(x, y) \quad (13)$$

The weight $w(x, y)$ represents the contribution of the element with higher brightness within the meta-granular ball, while the element with lower brightness is assigned a weight of $1 - w(x, y)$. Since the granular ball functions as a scale for computation, it estimates the contribution of the element carrying more informative content. As the computation is performed in the luminance space, elements with similar brightness levels tend to cause ambiguity in boundary and structural information. Therefore, according to Definition 4, the meta-granular balls containing such elements are categorized into the boundary domain (BND). Moreover, in Equation (9), the brighter element is adopted as the reference to avoid extreme computations caused by elements located near the boundaries of the granular ball during its sliding process.

After performing inference on all meta-granular balls, the ratio of those falling into the BND and the POS can be computed as follows:

$$r_{POS} = \text{count}(POS)/N \quad (14)$$

$$r_{BND} = \text{count}(BND)/N \quad (15)$$

where $\text{count}(POS)$ and $\text{count}(BND)$ represent the number of meta-granular balls that fall into the POS and BND, respectively, and N denotes the total number of meta-granular balls.

Definition 5. Modality Perception. The modality perception verifies whether $r_{POS} > 0.95$. If $r_{POS} < 0.95$, the weight $w(x, y)$ of the element with higher brightness in the meta-granular balls within the POS domain is set to 0.95, and both r_{POS} and r_{BND} are output. Otherwise, the weight $w(x, y)$ of the elements within the POS domain is set to 0.5, and the final values of r_{POS} and r_{BND} are assigned 0.5.

Finally, modality perception adaptively adjusts the modality under multi-exposure conditions according to Definition 5. Its empirical validation will be provided in the theoretical analysis section. The fusion weight of 0.95 is assigned solely to avoid extreme fusion, ensuring that the information from the other modality is preserved to a certain extent. After this process, the weight maps X_A and X_B corresponding to the input images are obtained, and the prior image is generated by weighted fusion as:

$$\text{Prior} = X_A \cdot A + X_B \cdot B, \quad (16)$$

where A and B denote the two input images from different modalities, and Prior represents the fused image used as the prior output. Here, X_A and X_B are the weight masks of the corresponding source images. Based on the above steps, the overall process of granular ball pixel computing is summarized in Algorithm 1.

Algorithm 1: Granular Ball Pixel Computing
Input: Two modality images A, B
Output: Prior fused image $Prior$, domain confidences r_{POS}, r_{BND}
Initialize: Meta-granular balls, step Δd , radius $r = \Delta d$, scale factor k ;

while there exist unclassified meta-granular balls in G **do**
if $r < k \Delta d$ **then**

 Expand granular ball;
 Slide the granular ball to capture nearby meta-granular balls;
 Classify captured ones into boundary domain BND ;
 Compute element weights inside each $mG \in BND$;

else

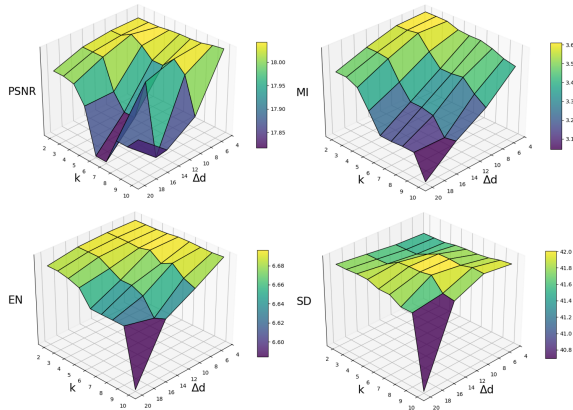
 Granular ball splitting;
 Assign current granular ball to positive domain POS ;
 Move captured meta-granular balls from BND to POS ;

 Compute r_{POS} and r_{BND} from the final partition;

Modality Perception;

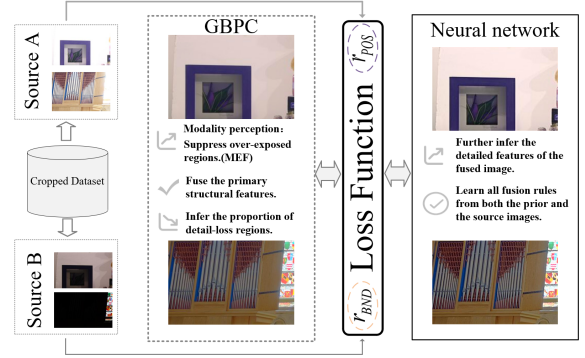
 Refine element weights within POS and update X_A, X_B ;

 Fuse prior image: $Prior \leftarrow X_A \cdot A + X_B \cdot B$;

return $Prior, r_{POS}, r_{BND}$;

 Fig. 4. Objective evaluation variations of the prior image under different values of k and Δd .

D. Parameters analysis

In Granular Ball Pixel Computing (GBPC), the parameters k and Δd jointly determine the perceptual domain and the splitting limit of each granular ball, thereby defining its overall scale. To ensure the robustness of the parameter configuration, we evaluated the quality of the prior images generated by the algorithm. At the algorithmic level, higher-quality prior images serve as the benchmark for determining the optimal values of k and Δd , and several evaluation metrics were measured,


 Fig. 5. The prior is obtained from the fragment library using Granular Ball Pixel Computing, and the loss function is dynamically adjusted according to r_{POS} and r_{BND} .

as shown in Fig.4. Comprehensive analysis of all evaluation metrics indicates that when $k = 6$ and $\Delta d = 10$, the prior images achieve the best overall performance across multiple indicators, demonstrating superior representational quality and algorithmic stability.

E. Few-shot learning

In our framework, unlike previous approaches, we integrate algorithmic inference and neural network inference to enable the network to learn a complete set of rules. The neural network is responsible for re-inferring the uncertain information in GBPC based on the existing prior. The entire process is carried out through a loss function, whose design dynamically adapts according to the prior image. In GBPC, the prior image represents an approximate inference. When calculating the elements of the meta-granular balls located in the BND, the edge information tends to become blurred. Therefore, the neural network re-infers the missing edge information from the source images based on the structural brightness of the prior image. The loss function is composed of three parts, and its overall formulation can be described as follows:

$$L_{total} = L_{SSIM} + L_{POS} + L_{BND}, \quad (17)$$

where L_{SSIM} transfers structural features from the prior image, L_{POS} conveys reliable edge information within the prior, and L_{BND} guides the network to infer weak regions of the prior based on feature extraction from the source images. The specific formulation of the loss function is defined as follows:

$$L_{SSIM} = 1 - SSIM(Out, Prior), \quad (18)$$

where Out denotes the fused output image generated by the network, and $Prior$ represents the prior image obtained through the Granular Ball Pixel Computing (GBPC).

$$L_{POS} = r_{POS} \times \mathcal{L}_1(\text{Sobel}(Out), \text{Sobel}(Prior)), \quad (19)$$

where r_{POS} denotes the proportion of the credible region in the prior image, which is also derived from GBPC. $\mathcal{L}_1(\cdot)$ represents the L1 loss function used to measure pixel-wise

differences, and $\text{Sobel}(\cdot)$ denotes the Sobel operator used for gradient extraction.

$$L_{\text{BND}} = r_{\text{BND}} \times \mathcal{L}_1(\text{Sobel}(\text{Out}), (\text{Sobel}(A) + \text{Sobel}(B))) + \mathcal{L}_1(\text{Lap}(\text{Out}), (\text{Lap}(A) + \text{Lap}(B))). \quad (20)$$

where r_{BND} represents the region with weaker edge responses in the prior image. This loss function assists the neural network in inferring correct regions from the source images A and B , where Lap denotes the Laplacian operator (second-order derivative) that helps to guide the reasoning of the first-order gradient extracted by the Sobel operator. Specifically, the Sobel and Laplacian operators mentioned above are as follows:

$$G_x = \begin{bmatrix} -1 & 0 & 1 \\ -2 & 0 & 2 \\ -1 & 0 & 1 \end{bmatrix}, \quad G_y = \begin{bmatrix} -1 & -2 & -1 \\ 0 & 0 & 0 \\ 1 & 2 & 1 \end{bmatrix}, \quad (21)$$

$$\text{Sobel}(I) = \sqrt{G_x^2 * I + G_y^2 * I}, \quad (22)$$

where G_x and G_y extract horizontal and vertical gradient features, respectively.

$$\text{Lap}(I) = \begin{bmatrix} 0 & 1 & 0 \\ 1 & -4 & 1 \\ 0 & 1 & 0 \end{bmatrix} * I, \quad (23)$$

IV. EXPERIMENTAL RESULTS AND ANALYSIS.

A. Experimental settings

To perform thorough validation, publicly available datasets were selected according to the requirements of each task. For the MEF (multi-exposure image fusion) task, we used the MEFB dataset. For the MFF (multi-focus image fusion) task, we used the Lytro dataset and the MFI-WHU dataset. For the VIF (infrared and visible image fusion) task, we used the M3FD, MSRS, RoadScene, and TNO datasets. For the MIF (medical image fusion) task, we used the Harvard (PET-MRI) dataset.

Regarding the composition of the training set, for the MEF task, we selected 10 images from the MEFB dataset as training samples. For the MFF task, we selected 10 images from the Lytro dataset. For the VIF task, we selected 5 image pairs from TNO dataset and 5 from MSRS dataset. For the MIF task, we selected 10 images from the Harvard (PET-MRI) dataset. These training images are not included in the test set.

All selected images were cropped into 128×128 patches with a stride of 64 to construct the crop dataset, and random flipping was applied during preprocessing. During training, the number of epochs was set to 100. To ensure fairness of comparison, all experiments were conducted on a computing platform equipped with an RTX 3090 GPU and an Intel i5-13600KF CPU.

B. Comparative Analysis

To verify the effectiveness of the proposed method, we selected three general-purpose fusion approaches and, for each specific task, additionally included four task-oriented fusion

methods for comparison. For clarity and ease of observation, the tasks associated with each comparative method are summarized in Table I. To ensure a fair comparison, all experiments were conducted on the same computing platform, and the implementations were reproduced using the model weights recommended by the original authors.

To conduct quantitative evaluation, we adopted several widely used objective metrics, including MI, EN, PSNR, VIF, SCD, Q_g , Qab, CC, and AG. Mutual Information (MI) measures how much information the fused image shares with the source images. Entropy (EN) evaluates the amount of information or the richness of details contained in the fused result. Peak Signal-to-Noise Ratio (PSNR) reflects the fidelity of the fused image with respect to a reference image. Visual Information Fidelity (VIF) assesses the visual quality of the fused image based on human visual perception. The Sum of Correlation Difference (SCD) quantifies how well the fused image preserves complementary information from the source images. The gradient-based quality metric (Q_g) evaluates the preservation of edges and structural details. The Qab metric (Qab) measures the amount of edge information transferred from the source images to the fused output. The Correlation Coefficient (CC) indicates the linear similarity between the fused image and each input image. Finally, the Average Gradient (AG) reflects the sharpness and texture richness of the fused result. For clearer observation, we annotate the objective evaluation metrics by marking the best scores in bold and the second-best scores with underlines.

1) *Multi-exposure image fusion*: For convenient comparison, we present the fusion results of different methods in Fig.6, where the detailed regions are further enlarged for visual examination. Compared with other approaches, our method effectively suppresses detail loss caused by overexposure while maintaining stable brightness without noticeable degradation. Among the displayed methods, our approach also achieves clearer text rendering, while the diffusion-based method (c) UltraFusion, although better preserving color vividness, shows partial disappearance of characters. As shown in Table II, our method achieves the best or second-best performance in MI, PSNR, CC, and Qab, indicating that it can preserve the original image information while maintaining superior overall image quality.

2) *Medical image fusion*: Figure 7 shows the fusion results produced by different methods, and for clearer observation, the regions rich in details are further enlarged. From the magnified regions of the fused images, we can observe that our method effectively preserves the color characteristics of the PET images while maintaining the complex structural details. The edges in the MRI images are also well preserved during the fusion process, which verifies the effectiveness of our method. As shown in Table II, our method achieves the best or second-best performance across all objective metrics, demonstrating its overall effectiveness.

3) *Multi-focus image fusion*: For convenient comparison, we present the fusion results of different methods in Fig.8, with enlarged views of detailed regions. In multi-focus image fusion, our method demonstrates superior performance in both edge features and fine structural details compared with other

TABLE I
COMPARISON OF DIFFERENT FUSION METHODS ON MEF, MFF, MIF, AND VIF TASKS.

Method	EAT[27]	SMAT[28]	UTFusion[13]	VDMU[29]	CCSR[30]	DMAnet[31]	GRFusion[32]	ZMFF[14]	TextFusion[33]	Coconet[34]	EMMA[35]	MMIF[18]	DDBFusion[36]	GifFusion[37]	U2Fusion[26]	Ours
Years	2025	2024	2025	2024	2025	2025	2023	2024	2025	2024	2024	2025	2025	2025	2020	–
MEF	✓	✓	✓	✓	×	×	×	×	×	×	×	×	×	✓	✓	✓
MFF	×	×	×	×	✓	✓	✓	✓	✓	✓	✓	✓	✓	✓	✓	✓
MIF	×	×	×	✓	×	×	×	×	×	✓	✓	✓	✓	✓	✓	✓
VIF	×	×	×	×	×	×	×	×	×	×	×	×	×	×	×	✓
Params (M)	0.016	1.233	556.805	31.773	0.039	4.076	7.71	4.66	0.074	6.845	1.52	0.749	10.921	7.71	0.659	0.015
FLOPs (G)	<u>1.522</u>	94.909	60659	188149	3.935	87.001	25.375	42.73	68.1	63.61	13.56	10.86	369.842	25.375	66.1	1.502
Times (ms)	5.843	5.386	88060	20304	52.481	15.152	12.75	9100	3.116	6.512	17.1	6.17	80.49	12.75	<u>3.016</u>	0.333

TABLE II
QUANTITATIVE COMPARISON ON MEFB AND HARVARD (PET-MRI) DATASETS.

Method	MEFB					Method	Harvard (PET-MRI)				
	EN	MI	PSNR	CC	Qab		MI	SD	PSNR	AG	Qab
EAT	6.819	6.207	10.378	0.880	0.598	VDMU	3.467	60.339	15.468	10.614	0.413
SAMT-MEF	6.949	4.792	<u>10.635</u>	<u>0.881</u>	<u>0.698</u>	COCOnet	2.570	62.769	11.852	15.437	0.479
UltraFusion	7.308	2.652	7.738	0.596	0.226	EMMA	2.991	85.119	<u>16.002</u>	17.512	0.696
VDMU	6.752	4.982	10.594	0.880	0.480	MMIF	3.009	87.985	15.573	<u>19.504</u>	<u>0.715</u>
BBDFFusion	<u>7.131</u>	4.604	10.412	0.875	0.458	BBDFFusion	2.927	69.864	15.121	13.051	0.374
GIFNet	<u>6.796</u>	4.288	10.618	0.858	0.291	GIFNet	2.629	79.149	14.448	15.930	0.457
U2Fusion	6.739	2.744	8.326	0.616	0.222	U2Fusion	2.726	62.874	15.400	8.397	0.287
OURS	6.938	<u>5.116</u>	10.638	0.883	0.708	OURS	<u>3.022</u>	<u>85.355</u>	16.010	20.282	0.717

TABLE III
QUANTITATIVE COMPARISON ON LYTRO AND MFI-WHU DATASETS.

Method	Lytro					MFI-WHU				
	EN	SD	VIF	SCD	CC	EN	SD	VIF	SCD	CC
CCSR-Net	7.531	57.565	<u>0.679</u>	0.840	0.971	7.319	52.379	<u>0.683</u>	0.868	0.967
DMANet	7.531	57.569	0.451	0.762	0.838	7.317	52.429	0.420	0.770	0.816
GRFusion	7.532	57.616	0.682	<u>0.841</u>	0.970	7.322	52.420	0.690	<u>0.872</u>	0.965
ZMFF	7.524	56.954	0.448	0.762	0.837	7.295	51.994	0.419	0.765	0.814
BBDFFusion	7.535	57.153	0.490	0.718	0.852	7.312	52.557	0.422	0.774	0.817
GIFNet	<u>7.598</u>	64.609	0.453	0.803	0.957	7.442	61.735	0.423	0.832	0.947
U2Fusion	7.460	58.390	0.492	0.710	0.849	7.226	53.326	0.422	0.766	0.815
OURS	7.634	<u>63.173</u>	0.533	0.842	0.974	<u>7.413</u>	59.004	0.522	0.874	0.968

TABLE IV
QUANTITATIVE COMPARISON ON M3FD AND MSRS DATASETS.

Method	M3FD					MSRS				
	MI	PSNR	VIF	SCD	Qg	MI	PSNR	VIF	SCD	Qg
TEXTFusion	<u>3.638</u>	16.390	0.379	0.731	0.833	3.745	20.040	0.411	0.702	0.757
COCOnet	2.715	12.513	0.312	0.743	0.735	2.205	11.212	0.324	0.657	0.617
EMMA	3.621	<u>16.375</u>	0.321	0.767	0.837	<u>3.952</u>	20.789	0.457	<u>0.740</u>	0.859
MMIF-INet	2.739	16.057	0.322	<u>0.783</u>	<u>0.852</u>	2.961	19.989	0.491	0.747	<u>0.862</u>
BBDFFusion	1.136	12.345	0.018	0.321	0.525	2.171	18.962	0.300	0.731	0.818
GIFNet	2.752	14.949	0.251	0.759	0.804	1.969	18.518	0.289	0.690	0.806
U2Fusion	2.818	15.591	0.251	0.781	0.782	2.146	18.745	0.249	0.730	0.685
OURS	3.778	16.077	<u>0.324</u>	0.785	0.857	3.997	<u>20.131</u>	<u>0.458</u>	0.752	0.869

approaches. It also maintains the vividness of the fused image consistent with the original inputs, which aligns with the proposed inference logic. Therefore, our method shows clear advantages in texture handling for multi-focus images. As shown in Table III, our approach achieves the best or second-best performance in EN, SD, SCD, and CC across different datasets. These results further verify the effectiveness of the proposed method.

4) *Infrared and visible image fusion:* Fig.9 presents the fusion results produced by different methods. For clearer visual inspection, the regions with rich details are further enlarged. The figure illustrates the fusion performance under various challenging conditions, including smoke, nighttime scenes, and lighting interference. Compared with other approaches, our method effectively preserves infrared features, which benefits from the GBPC-based prior that establishes the luminance foundation of the fused image, making the infrared characteristics more prominent. It also exhibits strong edge

responses, contributing to robust performance across diverse environments. As shown in Table IV and Table V, our method achieves the best results in MI, SCD, and Q_g , and obtains high or second-best scores on the remaining metrics. These results indicate that the proposed method can effectively preserve the edge structures and the original information in the fused images.

Although the proposed method adopts a few-shot learning strategy, it remains competitive when compared quantitatively and qualitatively with state-of-the-art approaches. This validates the effectiveness of our method. Under the guidance of the prior, the known prior information drives the neural network to extract complete fusion information from the source images, enabling the network to learn the entire fusion rule during this process. Consequently, the method avoids relying on large-scale datasets for gradual rule extraction and reduces the dependence of the neural network on the training data.

TABLE V
QUANTITATIVE COMPARISON ON ROADSCENE AND TNO DATASETS.

Method	RoadScene					TNO				
	MI	PSNR	VIF	SCD	Qg	MI	PSNR	VIF	SCD	Qg
TEXTFusion	3.537	16.378	0.373	0.778	0.682	3.428	15.464	0.418	0.770	0.821
COCONet	2.479	12.567	0.305	0.753	0.771	2.085	12.153	0.349	0.744	0.703
EMMA	3.291	14.626	0.360	0.790	0.812	3.038	14.815	0.397	0.788	0.839
MMIF-INet	2.626	16.206	0.348	0.785	<u>0.814</u>	2.407	15.420	0.392	0.789	<u>0.855</u>
BBDFusion	2.680	14.789	0.291	0.781	0.814	2.034	15.065	0.338	0.770	0.826
GIFNet	2.602	15.402	0.269	0.751	0.798	2.031	15.397	0.278	0.751	0.812
U2Fusion	3.025	16.429	0.305	0.774	0.800	2.110	15.901	0.292	<u>0.792</u>	0.804
OURS	3.610	16.016	0.337	0.791	0.826	3.630	15.168	0.422	0.794	0.867

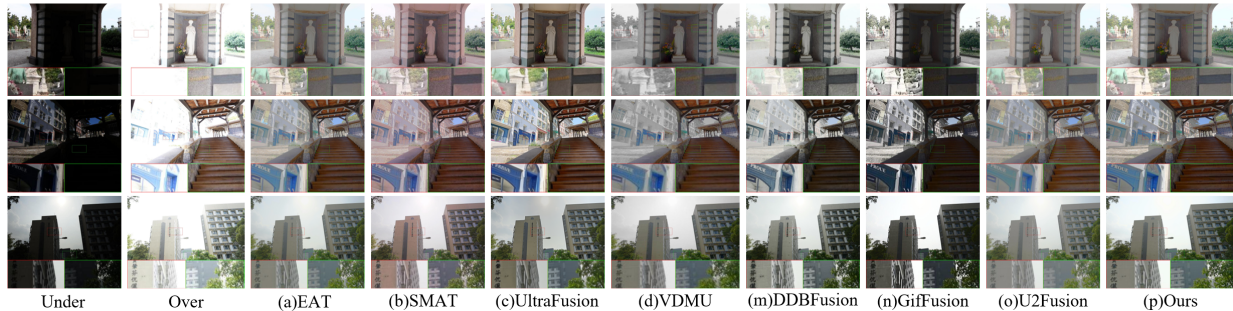


Fig. 6. Qualitative comparison of fused results obtained by different methods on the MEF task.

C. Efficiency Analysis

We conducted experiments to evaluate the parameter size, FLOPs, and fusion time of different models. All experiments were performed using input images of size 224×224 , and each model was executed 100 times, with the average value taken as the final result. As shown in Table I, our method achieves the best performance in parameter count, FLOPs, and fusion time. In our framework, the neural network infers the edge features of the true fused image based on an incomplete but known prior. Therefore, the network architecture remains lightweight and is implemented as a clean CNN without requiring additional regularization structures to assist the inference process. In contrast, other methods, such as diffusion-based models or deep network architectures, incur significantly higher computational costs. These results demonstrate that the proposed method has strong deployability and practical efficiency advantages.

V. ABLATION STUDY AND THEORETICAL ANALYSIS

A. Incomplete prior and few-shot learning

We construct the prior based on the equivalence principle in rough set theory, which enables the GBPC algorithm to produce an incomplete prior. Unlike conventional hand-crafted fusion methods that generate a fully fused result, the GBPC prior is closer to a degenerated fusion image: it preserves only the modality-consistent structural information while intentionally leaving uncertain components unresolved. Therefore, the GBPC prior does not attempt to accomplish the fusion task; instead, it provides structural cues to guide the subsequent learning stage as an incomplete prior. Different from conventional weakly supervised learning, the prior in our framework is not intended to provide coarse fusion guidance, but to reduce the reasoning burden of the network. To this end, we design a loss function dynamically regulated by the

GBPC prior, where the positive domain (POS) and boundary domain (BND) represent deterministic and uncertain regions, respectively. Accordingly, the loss adaptively guides the network to: trust the structural cues in reliable regions, and re-infer ambiguous edges and details from the source modalities in uncertain regions, rather than directly imitating the prior.

In contrast, traditional fusion algorithms generate complete priors. Such methods usually impose strong algorithmic preferences and provide a fully-constructed fusion image to the network. When a complete prior is injected into the model, it becomes difficult for the network to distinguish informative cues from algorithm-induced biases, leading the network to inherit the shortcomings of the prior during training and eventually weakening the fusion performance. To validate the effectiveness of loss propagation and re-inference driven by an incomplete prior, we replace the GBPC prior with four representative complete priors. Specifically, we adopt: Curvelet (based on the curvelet transform), DTCWT (utilizing the dual-tree complex wavelet transform), GFF (using guided filtering), and LP (based on Laplacian pyramid decomposition). Since these priors do not provide an uncertainty ratio, we uniformly set their loss parameters as $r_{POS} = r_{BND} = 0.5$ and train them under identical small-sample settings. As shown in Fig. 10 and Table VI, networks guided by complete priors inherit method-specific artifacts, such as dark overstaining in MEF, even when the network attempts to refine edges from the source images. In contrast, the GBPC prior keeps uncertain regions through the BND and allows the network to continue reasoning instead of committing to an erroneous fusion pattern. Consequently, our approach achieves superior qualitative and quantitative results.

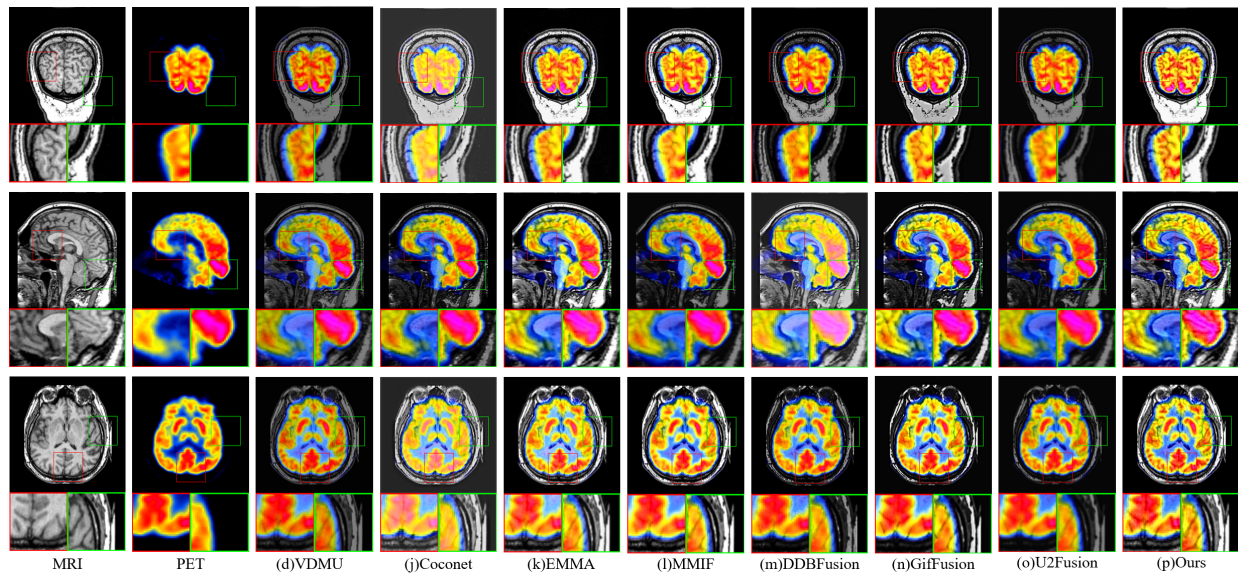


Fig. 7. Qualitative comparison of fused results obtained by different methods on the MIF task.



Fig. 8. Qualitative comparison of fused results obtained by different methods on the MFF task.



Fig. 9. Qualitative comparison of fused results obtained by different methods on the VIF task.

TABLE VI
PERFORMANCE COMPARISON OF TRADITIONAL PRIORS, GBPC, AND THE PROPOSED METHOD ACROSS MEF, MIF, MFF, AND VIF TASKS.

Method	MEF					MIF					MFF					VIF				
	EN	MI	PSNR	CC	Qab	MI	PSNR	VIF	SCD	Qg	MI	SD	PSNR	AG	Qab	EN	SD	VIF	SCD	CC
Curvelet	6.491	3.995	8.500	0.459	<u>0.697</u>	3.316	15.950	0.255	0.695	0.808	<u>2.975</u>	77.412	15.349	18.461	0.676	7.098	59.972	0.451	0.758	0.896
Curvelet_prior	5.627	3.758	9.272	<u>0.673</u>	0.346	3.209	16.022	0.237	0.715	0.814	2.695	79.614	14.217	17.923	0.656	7.130	58.340	0.404	0.804	0.934
Dtcwt	6.448	<u>5.006</u>	7.974	0.497	0.667	3.278	15.486	0.240	0.704	0.809	2.840	77.450	<u>15.309</u>	18.513	0.689	7.141	59.647	0.500	0.763	0.889
Dtcwt_prior	5.463	3.475	9.013	0.651	0.285	3.129	15.659	0.227	0.720	0.811	2.513	74.507	<u>14.268</u>	17.026	0.650	<u>7.284</u>	58.385	0.470	<u>0.806</u>	0.926
GFF	6.316	3.739	8.197	0.440	0.693	<u>3.508</u>	16.169	0.375	0.689	0.809	2.877	77.470	15.311	18.466	<u>0.690</u>	6.983	58.010	<u>0.510</u>	0.764	0.890
GFF_prior	<u>6.843</u>	3.588	8.158	0.626	0.676	3.202	15.904	0.252	0.700	0.814	2.640	<u>80.097</u>	14.677	19.266	0.676	7.060	58.214	0.417	0.795	<u>0.949</u>
Lp	6.452	4.940	8.491	0.428	0.660	2.549	15.455	0.297	0.713	0.796	2.910	77.775	15.246	18.574	0.682	7.156	<u>60.184</u>	0.509	0.768	0.871
Lp_prior	5.343	3.600	<u>9.273</u>	0.628	0.298	3.133	15.838	0.237	<u>0.721</u>	0.819	2.590	77.167	13.946	<u>19.735</u>	0.660	7.245	59.422	0.460	0.790	0.890
GBPC	6.636	4.495	8.370	0.582	0.476	3.690	<u>16.407</u>	<u>0.377</u>	0.671	<u>0.828</u>	2.203	74.628	13.015	16.393	0.584	6.870	58.863	0.443	0.743	0.921
OURS	6.938	5.116	10.638	0.883	0.708	3.795	16.864	0.382	0.779	0.863	3.022	85.355	16.010	20.282	0.717	7.524	61.088	0.528	0.858	0.971

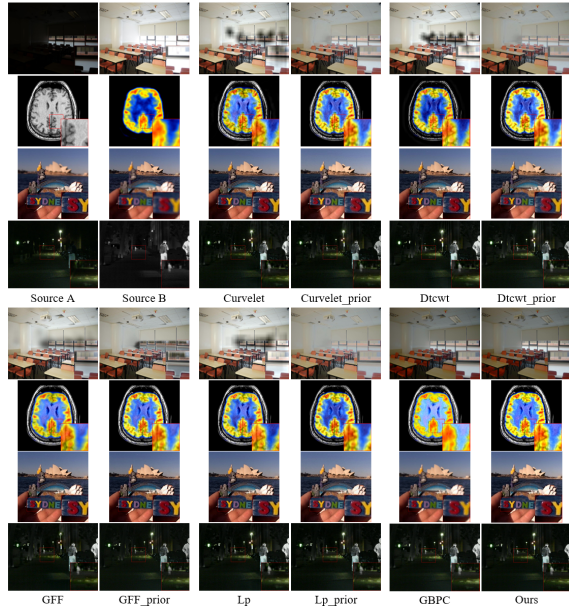


Fig. 10. Visualization of fused results produced by different algorithms, along with the fused images obtained when these results are further used as priors for the neural network.

B. Influence of prior confidence

In the GBPC algorithm, we compute the confidence of the prior to guide the design of the loss function. To investigate how this computation influences the network’s re-inference process, we perturb the output values of r_{pos} and r_{bnd} . Specifically, we set up three groups of controlled experiments: (1) $r_{POS} = 1$, $r_{BND} = 0$; (2) $r_{POS} = 0.5$, $r_{BND} = 0.5$; (3) $r_{POS} = 0$, $r_{BND} = 1$. The experimental results are shown in Table VII, where a quantitative evaluation of the fused images is provided. It can be observed that, due to the network’s insufficient response to ambiguous regions, the fusion performance across multiple tasks is inferior to that of the guided method. This validates the rationality of the confidence computed by GBPC, demonstrating that it effectively guides the network to extract edge features from the source images.

C. Modality awareness

In the GBPC algorithm, we incorporate the parameters r_{POS} and r_{BND} to enable modality-aware perception of high-exposure regions. This mechanism strengthens texture information in locally similar areas while suppressing regions

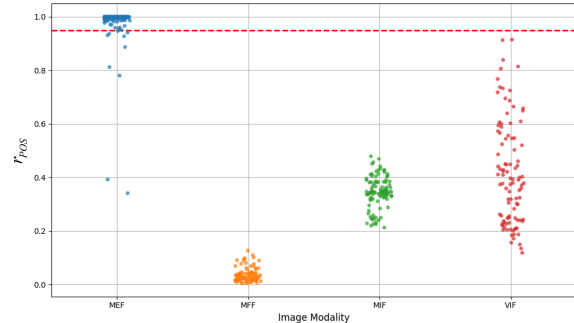


Fig. 11. Distribution of r_{POS} measured by applying the GBPC algorithm to 100 randomly selected images from each modality. The red dashed line represents 0.95.

with excessively high intensity. In this section, we verify the modality-awareness property from a statistical perspective. As shown in Fig. 11, we randomly sample 100 image pairs from multiple datasets and compute the distribution of r_{POS} . It can be observed that, across different modalities, when the threshold is set to $r_{POS} = 0.95$, the images from the other modality do not fall within the interval $(0.95, 1)$. This demonstrates that the proposed algorithm can effectively suppress high-exposure regions. It is important to note that this suppression effect applies only to strongly over-exposed areas. In regions where the intensities are similar, the algorithm still enhances structural information; hence, although some high-exposure images do not fall within the interval $(0.95, 1)$, the resulting prior remains effective for guiding the neural network. In the subsequent ablation study (Table VII), we further conduct quantitative analysis. Modality perception only applies to MEF, so we report MEF metrics only. The results show that priors lacking modality-awareness fail to adequately suppress high-exposure regions and yield inferior performance on objective evaluation metrics.

D. Loss function ablation

In our framework, the prior is connected through the loss function, and the loss terms are adjusted to encourage the network to extract edge information from the source images. In this section, we conduct an ablation study on the loss function, specifically including: (1) **w/o L_{POS}** : removing the extraction of edge information from the prior; (2) **w/o L_{BND}** : removing the extraction of edge features from the source images; (3) **w/o Laplacian**: removing the second-order derivative used for auxiliary inference. The quantitative

TABLE VII
ABLATION RESULTS ACROSS MEF, MIF, MFF, AND VIF TASKS.

Method	MEF					MIF					MFF					VIF				
	EN	MI	PSNR	CC	Qab	MI	PSNR	VIF	SCD	Qg	MI	SD	PSNR	AG	Qab	EN	SD	VIF	SCD	CC
$r_{POS} = 0.5, r_{BND} = 0.5$	6.470	4.925	9.858	0.872	0.632	3.772	16.051	0.340	0.720	0.860	2.953	79.885	15.665	18.719	0.668	7.405	57.684	0.515	0.850	0.961
$r_{POS} = 0, r_{BND} = 1$	6.545	4.234	9.871	0.861	0.680	3.688	15.936	0.319	0.627	0.853	2.884	81.075	15.417	18.600	0.705	7.466	59.763	0.512	0.837	0.954
$r_{POS} = 1, r_{BND} = 0$	6.390	5.048	9.027	0.875	0.473	3.704	16.418	0.339	0.716	0.853	3.005	73.393	15.895	14.674	0.566	7.394	58.019	0.519	0.838	0.959
w/o L_{POS}	6.333	4.177	9.867	0.838	0.572	3.638	16.162	0.319	0.720	0.855	2.935	74.046	15.929	16.127	0.524	7.436	60.060	0.497	0.834	0.955
w/o L_{BND}	6.477	4.757	9.858	0.867	0.552	3.626	16.337	0.269	0.728	0.854	2.910	74.783	15.027	16.136	0.523	7.362	59.654	0.500	0.833	0.953
w/o $Laplacian$	6.618	4.293	9.922	0.869	0.701	3.616	15.767	0.331	0.727	0.862	2.786	81.334	15.820	18.864	0.701	7.484	60.977	0.508	0.842	0.954
w/o Modality Perception	6.245	5.021	8.125	0.812	0.651	-	-	-	-	-	-	-	-	-	-	-	-	-	-	-
OURS	6.938	5.116	10.638	0.883	0.708	3.795	16.864	0.382	0.779	0.863	3.022	85.355	16.010	20.282	0.717	7.524	61.088	0.528	0.858	0.971

results are shown in Table VII. It can be observed that, when the source-image edge features are removed, the fused images exhibit degraded performance. When the prior-image edge information is omitted, the network lacks part of the necessary structural cues, resulting in incomplete information and suboptimal fusion outcomes. In contrast, incorporating the second-order derivative significantly improves the image quality, which validates the rationality and effectiveness of the designed loss function.

E. Influence of Sample Size

In this section, we investigate the influence of sample size on the performance of few-shot learning. We construct several comparison groups with different numbers of training samples, specifically: 1_shot , 5_shot , 10_shot (ours), 15_shot , and 20_shot . To ensure consistency across experiments, the selected samples follow an inclusion relationship, i.e., the 15_shot subset is contained within the 20_shot set. For each configuration, multiple random sampling trials are conducted, and the final results are obtained by averaging the objective evaluation metrics. All experimental settings, including the number of iterations, remain identical, and the sample size serves as the only varying factor. As illustrated in Fig. 12, all metrics are normalized to the range (0,1) for clearer visualization. The results show that when the sample size is extremely limited, such as in the 1_shot and 5_shot settings, the generalization capability is significantly weakened. When the sample size exceeds 10, the objective metrics begin to stabilize, though mild fluctuations are still observed. This indicates that although our framework incorporates rule-based priors, the neural network still requires a minimum amount of data to effectively learn and enhance generalization. Moreover, in our framework, the neural network must not only utilize the provided prior but also infer additional edge features from the source images. This necessitates a minimal number of training samples to ensure that the model can learn robust fusion rules and simulate real-world scenarios even from limited image fragments.

F. Limitations

In the proposed method, we expect the neural network to continue reasoning based on the available prior, thereby compensating for the incompleteness of the prior. Although the experimental results demonstrate that the proposed method exhibits good generalization ability, several issues remain unresolved in the current experiments. Specifically:

I. The prior is provided by the GBPC algorithm, which is primarily suitable for typical image fusion tasks. For broader future applications, additional subspaces may be required to enable further inference.

II. The few-shot learning strategy in this work relies on image cropping to simulate various conditions, allowing the adaptive prior-generation algorithm to reconstruct fusion rules on cropped images. This design shifts the network’s learning paradigm from extracting features solely from the dataset to re-inference based on the prior, thereby reducing reliance on large datasets. However, if the few-shot dataset contains overly extreme samples, the learned weights may exhibit reduced generalization capability.

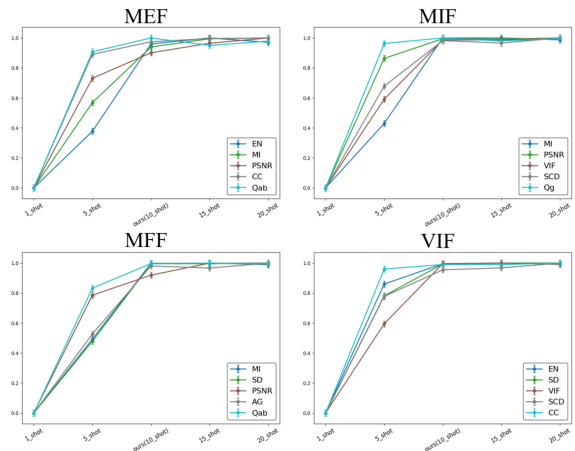


Fig. 12. Quantitative analysis of fused images on different tasks under varying numbers of training samples.

VI. CONCLUSION

In this work, we design a few-shot learning framework for general-purpose image fusion by introducing an incomplete prior that drives the neural network to perform re-inference. Instead of directly learning from the source images, the network is guided to infer the ambiguous structures contained in the prior, thereby learning fusion rules through a loss function and substantially reducing its dependence on large-scale training datasets. Specifically, based on rough set theory, we propose the granular ball pixel computing (GBPC) algorithm, which computes fusion weights at a fine granularity with modality awareness and evaluates prior effectiveness at a coarse granularity. This enables the loss function to be dynamically adjusted during training, guiding the network toward more effective inference. Comprehensive experiments, including

comparisons with state-of-the-art methods, demonstrate the effectiveness of the proposed framework. We further analyze the differences between complete priors and incomplete priors, and validate the effectiveness of prior transmission through controlled experiments. In addition, the modality-awareness mechanism and the dynamic adjustment of the loss function are shown to be essential components through dedicated ablation studies. The influence of sample size on the proposed few-shot learning paradigm is also examined, revealing that a minimal number of samples is necessary for stable and generalizable learning. Finally, we discuss the limitations of the proposed approach. In future work, we plan to incorporate additional subspaces to enhance accuracy and expressiveness, and extend the framework to broader image processing tasks such as image segmentation and super-resolution.

REFERENCES

- [1] J. Liu, G. Wu, Z. Liu, D. Wang, Z. Jiang, L. Ma, W. Zhong, X. Fan, and R. Liu, "Infrared and visible image fusion: From data compatibility to task adaption," *IEEE Transactions on Pattern Analysis and Machine Intelligence*, vol. 47, no. 4, pp. 2349–2369, 2025.
- [2] X. Zhang, "Deep learning-based multi-focus image fusion: A survey and a comparative study," *IEEE Transactions on Pattern Analysis and Machine Intelligence*, vol. 44, no. 9, pp. 4819–4838, 2022.
- [3] A. P. James and B. V. Dasarthy, "Medical image fusion: A survey of the state of the art," *Information fusion*, vol. 19, pp. 4–19, 2014.
- [4] H. Zhang, H. Xu, X. Tian, J. Jiang, and J. Ma, "Image fusion meets deep learning: A survey and perspective," *Information Fusion*, vol. 76, pp. 323–336, 2021.
- [5] S. Li, X. Kang, and J. Hu, "Image fusion with guided filtering," *IEEE Transactions on Image Processing*, vol. 22, no. 7, pp. 2864–2875, 2013.
- [6] Y. Liu, S. Liu, and Z. Wang, "A general framework for image fusion based on multi-scale transform and sparse representation," *Information fusion*, vol. 24, pp. 147–164, 2015.
- [7] H. Li and X.-J. Wu, "Densefuse: A fusion approach to infrared and visible images," *IEEE Transactions on Image Processing*, vol. 28, no. 5, pp. 2614–2623, 2018.
- [8] K. Ram Prabhakar, V. Sai Srikar, and R. Venkatesh Babu, "Deepfuse: A deep unsupervised approach for exposure fusion with extreme exposure image pairs," in *Proceedings of the IEEE international conference on computer vision*, 2017, pp. 4714–4722.
- [9] J. Ma, W. Yu, P. Liang, C. Li, and J. Jiang, "Fusiongan: A generative adversarial network for infrared and visible image fusion," *Information fusion*, vol. 48, pp. 11–26, 2019.
- [10] J. Ma, H. Xu, J. Jiang, X. Mei, and X.-P. Zhang, "Ddcgan: A dual-discriminator conditional generative adversarial network for multi-resolution image fusion," *IEEE Transactions on Image Processing*, vol. 29, pp. 4980–4995, 2020.
- [11] K. Han, Y. Wang, H. Chen, X. Chen, J. Guo, Z. Liu, Y. Tang, A. Xiao, C. Xu, Y. Xu *et al.*, "A survey on vision transformer," *IEEE transactions on pattern analysis and machine intelligence*, vol. 45, no. 1, pp. 87–110, 2022.
- [12] J. Ma, L. Tang, F. Fan, J. Huang, X. Mei, and Y. Ma, "Swinfusion: Cross-domain long-range learning for general image fusion via swin transformer," *IEEE/CAA Journal of Automatica Sinica*, vol. 9, no. 7, pp. 1200–1217, 2022.
- [13] Z. Chen, Y. Wang, X. Cai, Z. You, Z. Lu, F. Zhang, S. Guo, and T. Xue, "Ultrafusion: Ultra high dynamic imaging using exposure fusion," in *Proceedings of the Computer Vision and Pattern Recognition Conference (CVPR)*, June 2025, pp. 16 111–16 121.
- [14] X. Hu, J. Jiang, X. Liu, and J. Ma, "Zmff: Zero-shot multi-focus image fusion," *Information Fusion*, vol. 92, pp. 127–138, 2023.
- [15] H. Zhai, M. Deng, Y. Wei, L. Wang, and A. Li, "Zvir: Zero-shot implicit deep image prior with prior activation for infrared and visible image fusion," *Pattern Recognition*, p. 112666, 2025.
- [16] H. Bai, Z. Zhao, J. Zhang, Y. Wu, L. Deng, Y. Cui, B. Jiang, and S. Xu, "Refusion: Learning image fusion from reconstruction with learnable loss via meta-learning," *International Journal of Computer Vision*, vol. 133, no. 5, pp. 2547–2567, 2025.
- [17] Z. Wang, L. Zhao, J. Zhang, R. Song, H. Song, J. Meng, and S. Wang, "Multi-text guidance is important: Multi-modality image fusion via large generative vision-language model," *International Journal of Computer Vision*, pp. 1–23, 2025.
- [18] D. He, W. Li, G. Wang, Y. Huang, and S. Liu, "Mmif-inet: Multimodal medical image fusion by invertible network," *Information Fusion*, vol. 114, p. 102666, 2025.
- [19] W. Wang, L.-J. Deng, and G. Vivone, "A general image fusion framework using multi-task semi-supervised learning," *Information Fusion*, vol. 108, p. 102414, 2024.
- [20] H. Kang, H. Li, T. Xu, X.-J. Wu, R. Wang, C. Cheng, and J. Kittler, "Smlnet: A spd manifold learning network for infrared and visible image fusion," *International Journal of Computer Vision*, pp. 1–22, 2025.
- [21] S. Cheng, X. Su, B. Chen, H. Chen, D. Peng, and Z. Yuan, "Gbmmod: A granular-ball mean-shift outlier detector," *Pattern Recognition*, vol. 159, p. 111115, 2025.
- [22] S. Xia, C. Wang, G. Wang, X. Gao, W. Ding, J. Yu, Y. Zhai, and Z. Chen, "Gbrs: A unified granular-ball learning model of pawlak rough set and neighborhood rough set," *IEEE Transactions on Neural Networks and Learning Systems*, 2023.
- [23] S. Xia, H. Zhang, W. Li, G. Wang, E. Giem, and Z. Chen, "Gbnrs: A novel rough set algorithm for fast adaptive attribute reduction in classification," *IEEE Transactions on Knowledge and Data Engineering*, vol. 34, no. 3, pp. 1231–1242, 2020.
- [24] S. Xia, D. Peng, D. Meng, C. Zhang, G. Wang, E. Giem, W. Wei, and Z. Chen, "Ball k k-means: Fast adaptive clustering with no bounds," *IEEE transactions on pattern analysis and machine intelligence*, vol. 44, no. 1, pp. 87–99, 2020.
- [25] J. Xie, W. Kong, S. Xia, G. Wang, and X. Gao, "An efficient spectral clustering algorithm based on granular-ball," *IEEE Transactions on Knowledge and Data Engineering*, vol. 35, no. 9, pp. 9743–9753, 2023.
- [26] H. Xu, J. Ma, J. Jiang, X. Guo, and H. Ling, "U2fusion: A unified unsupervised image fusion network," *IEEE transactions on pattern analysis and machine intelligence*, vol. 44, no. 1, pp. 502–518, 2020.
- [27] W. Tang and F. He, "Eat: Multi-exposure image fusion with adversarial learning and focal transformer," *IEEE Transactions on Multimedia*, vol. 27, pp. 3744–3754, 2025.
- [28] Q. Huang, G. Wu, Z. Jiang, W. Fan, B. Xu, and J. Liu, "Leveraging a self-adaptive mean teacher model for semi-supervised multi-exposure image fusion," *Information Fusion*, p. 102534, 2024.
- [29] Y. Shi, Y. Liu, J. Cheng, Z. J. Wang, and X. Chen, "Vdmufusion: A versatile diffusion model-based unsupervised framework for image fusion," *IEEE Transactions on Image Processing*, vol. 34, pp. 441–454, 2025.
- [30] K. Zheng, J. Cheng, and Y. Liu, "Unfolding coupled convolutional sparse representation for multi-focus image fusion," *Information Fusion*, vol. 118, p. 102974, 2025.
- [31] Y. Quan, X. Wan, Z. Tang, J. Liang, and H. Ji, "Multi-focus image fusion via explicit defocus blur modelling," in *Proceedings of the AAAI Conference on Artificial Intelligence*, vol. 39, no. 6, 2025, pp. 6657–6665.
- [32] H. Li, D. Wang, Y. Huang, Y. Zhang, and Z. Yu, "Generation and recombination for multifocus image fusion with free number of inputs," *IEEE Transactions on Circuits and Systems for Video Technology*, vol. 34, no. 7, pp. 6009–6023, 2023.
- [33] C. Cheng, T. Xu, X.-J. Wu, H. Li, X. Li, Z. Tang, and J. Kittler, "Textfusion: Unveiling the power of textual semantics for controllable image fusion," *Information Fusion*, vol. 117, p. 102790, 2025.
- [34] J. Liu, R. Lin, G. Wu, R. Liu, Z. Luo, and X. Fan, "Coconet: Coupled contrastive learning network with multi-level feature ensemble for multi-modality image fusion," *International Journal of Computer Vision*, vol. 132, no. 5, pp. 1748–1775, 2024.
- [35] Z. Zhao, H. Bai, J. Zhang, Y. Zhang, K. Zhang, S. Xu, D. Chen, R. Timofte, and L. Van Gool, "Equivariant multi-modality image fusion," in *Proceedings of the IEEE/CVF conference on computer vision and pattern recognition*, 2024, pp. 25 912–25 921.
- [36] Z. Zhang, H. Li, T. Xu, X.-J. Wu, and J. Kittler, "Ddbfusion: A unified image decomposition and fusion framework based on dual decomposition and bézier curves," *Information Fusion*, vol. 114, p. 102655, 2025.
- [37] C. Cheng, T. Xu, Z. Feng, X. Wu, Z. Tang, H. Li, Z. Zhang, S. Atito, M. Awais, and J. Kittler, "One model for all: Low-level task interaction is a key to task-agnostic image fusion," in *Proceedings of the Computer Vision and Pattern Recognition Conference*, 2025, pp. 28 102–28 112.